UNIVERSITY OF CALIFORNIA
Santa Barbara

Determining Phase Stability in the Co-Al-W System using First Principles Methods

A thesis submitted in partial satisfaction
of the requirements for the degree of

Master of Science

in

Materials

by

Philip C. Dodge

Committee in Charge:

Professor Matthew Begley, Chair

Professor Anton Van der Ven

Professor Tresa Pollock

September 2015

The thesis of
Philip C. Dodge
is approved:

Professor Anton Van der Ven

Professor Tresa Pollock

Professor Matthew Begley, Committee Chairman

June 2015

Acknowledgements

Much thanks to the Anton Van der Ven group, both at the University of Michigan and UC Santa Barbara: none of this would be possible without such great collaborators.

An especially warm thank you to Anirudh Natarajan, John Goiri and Ivy Chen for the boundless patience and tenacity they have shown.

Thanks also to my officemates, Will Pro, Stephen Sehr, and Steven Wehmeyer, for their conversations, encouragements, and computer help.

I owe so much to my advisors, Matt Begley, Tresa Pollock, and Anton Van der Ven, as well as the many amazing professors at UCSB from which I have had the pleasure of learning.

"Perhaps only in a world of the blind will things be what they truly are."
-José Saramago

Abstract

Determining Phase Stability in the Co-Al-W System using First Principles Methods

Philip C. Dodge

Co-based superalloys are a promising new material for high strength, high temperature applications due to their γ-γ' microstructure. Within the Co-Al-W ternary system, the γ' phase manifests as an $L1_2$ structure in a small temperature range. Determining the thermodynamic stability of the $L1_2$ phase relative to other phases in this system is important for guiding the alloy development process. Density functional theory allows the direct calculation of free energy for these phases. The configurational energy component of the energy for the $L1_2$ structure was calculated via a cluster expansion, and the vibrational energy component for all structures was calculated in the quasiharmonic approximation. The results show that the $L1_2$ structures become stable at 600K and increase stability at higher temperatures, which has not been shown in previous work.

The purpose of this thesis is both to show the encouraging research results in the Co-Al-W system, and also to be a useful guide for performing first principles calculations and connecting theory, VASP usage, and the utilization of the CASM code.

Contents

1 Introduction

1.a Turbine blades & superalloy development

The turbine blades inside jet engines and natural gas stationary power generators experience some of the most extreme man-made environments. Air and fuel are compressed by fans before being ignited right before the turbine section of the engine. The job of the turbine blades is to turn this high-pressure, high-temperature explosion into useable energy, be it thrust or electricity. The spinning blades result in high tensile stresses. The combination of high temperature and high stresses creates a perfect environment for creep to occur. Thus, one of the main goals for material selection of the bulk of the turbine blade is a material's ability to avoid creep.

Nickel superalloys have been the premier choice in this application for many decades. With its high melting temperature of 1455°C , nickel is an excellent base for a high-temperature alloy. Nickel superalloys' unique microstructure allows it to operate at 90% of its melting temperature in chemically extreme environments [1]. This microstructure, called γ-γ' , may be thought of as a brick and mortar structure consisting of a cuboidal γ' phase with a relatively softer γ phase surrounding the bricks. Under deformation, the narrow γ channels are thought to restrict the motion of dislocations, resulting in high strength and excellent creep properties.

The fuel efficiency of a turbine engine increases with its operating temperature. This provides tremendous financial incentive to develop turbine blades that can operate at higher and higher temperatures. Significant alloy development in the past 60 years has resulted in+300°C operating temperatures. Figure 1 shows the creep lifetime for the many nickel superalloys developed in the past decades, and also shows the decelerating advancements in temperature. These latest alloys are reaching the fundamental limit of nickel's melting temperature.

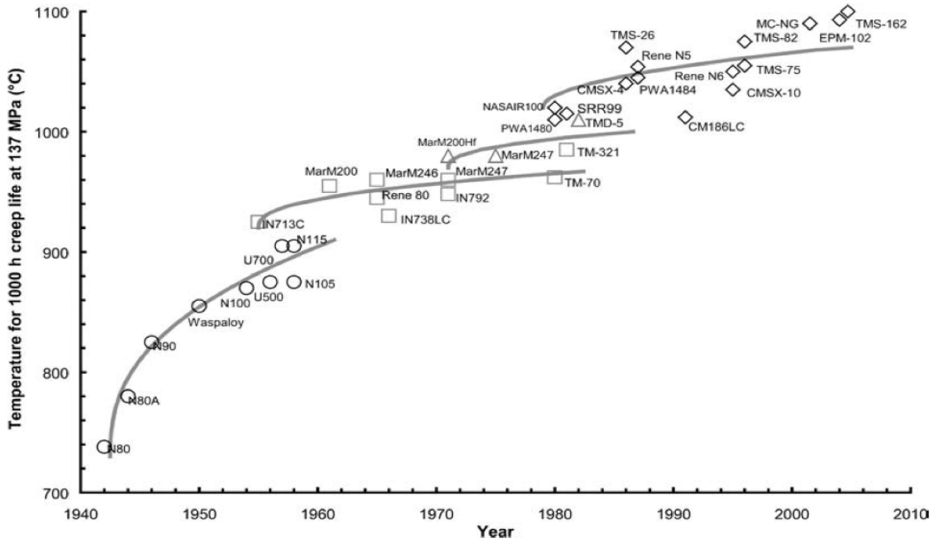

Figure 1: Creep life for selected nickel-based superalloys by year of development. The different point shapes refer to, by increasing temperature: wrought, conventionally cast, directionally solidified, and single crystal alloys.

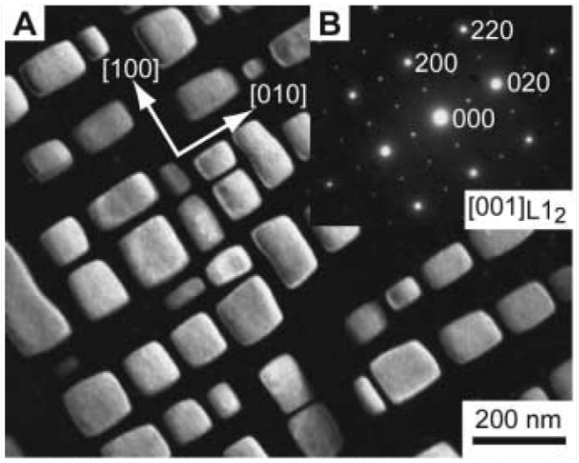

Figure 2: Electron micrograph of Co-9Al-7.5W alloy showing (a) dark-field image and (b) selected area diffraction pattern [2].

In 2006, Sato et al. [2] discovered that a Co-9Al-7.5W alloy exhibited the same γ-γ' microstructure as the nickel superalloys. This sparked a new wave of research, encouraged by cobalt's +40°C melting temperature advantage over nickel. Figure 2 shows a dark-field micrograph of the γ-γ' microstructure in a Co-alloy, where the γ' cuboidal particles are seen in clear contrast to the dark γ . The discovery of this same γ-γ' microstructure means that Co-based superalloys may be a direct competitor to current Ni-based superalloys. However, with less than ten years development in Co superalloys, much more basic research is required.

In previous years, alloy development would consist of many laborious tests and an iterative experimental process of adding/subtracting alloying additions over the course of decades of research. The advent of computational methods allows us to gain a greater

understanding of the underlying processes governing an alloy system, as well as the ability to sample a large compositional space in a reduced amount of time. Density functional theory allows us to explore the relative stability of phases relevant to Co-based superalloys, based on first principles rather than experimental inputs.

1.b Co-Al-W Ternary System

From Sato et al. [2] we know that the γ-γ' microstructure occurs in the Co-Al-W ternary system. At present, there is great debate about whether the γ' phase in this system is stable or metastable [3]. Because the γ' phase is so critical to the high temperature mechanical properties of a superalloy, its stability relative to other phases is important to understand.

Figure 3 shows an experimental Co-Al-W ternary phase diagram with γ' occuring in a small sliver of compositional space. It also shows some important phases that show up in this system. The γ phase is an fcc solid solution, while the γ' phase has an $L1_2$ structure. An $L1_2$ structure is an fcc cell with the corner atoms replaced by an alloying addition(s), in this case Al and W. Figure 4 shows an image of this $L1_2$-$Co_3(Al,W)$ cell. The experimental phase diagram appears to indicate some solubility of Co on the corner, "B", sublattice, because the $L1_2$ phase exists at >75% total Co.

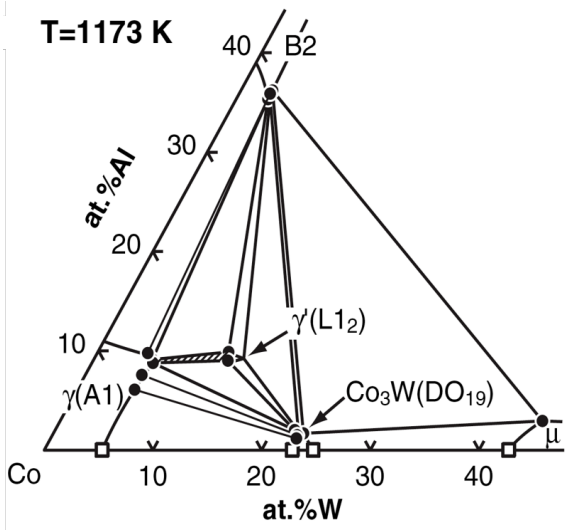

Figure 3: Experimental phase diagram of the Co-rich portion of the Co-Al-W ternary system at 1173K [2].

Also present in Figure 3 is the $D0_{19}$-Co_3W phase, with a hexagonal-based unit cell. The B2-CoAl phase is based off of a bcc cell. Not shown is the hcp-Co phase. The

hcp-Co phase is experimentally found to be stable below 690K [4] but undergoes an hcp to fcc transition above this temperature. The μ phase shows up in experiments but is not within the compositional space of the $L1_2$ phase, so it is ignored in this work. It has a complicated, very non-cubic 13 atom primitive cell.

Understanding the thermodynamic stability between all these phases is an important first step in establishing a computational framework for working in this, and other Co-based, alloy systems. In any phase, there are three energy contributions that usually dominate: the formation energy, the configurational energy, and the vibrational energy. The first is the energy difference between a compound and its constituent elements alone. The configurational energy exists based on the solubility of alloying additions in a structure. The vibrational energy is the action of phonons in the material: the main source of thermal energy present when a phase is at elevated temperature. Being able to calculate these energy contributions computationally will give critical insight into the relative thermodynamic stability between all these phases.

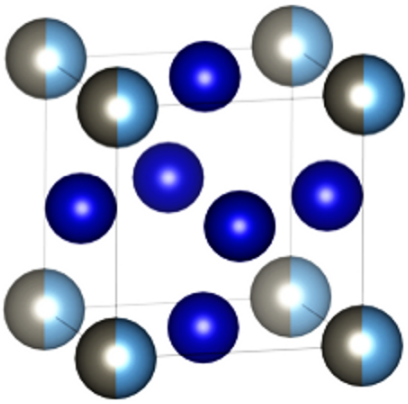

Figure 4: $L1_2$-Co_3(Al,W) unit cell with variable Al-W sublattice at corners.

2 Basic Structures

This section introduces basic VASP usage and how to calculate formation energies.

2.a VASP Introduction

The Vienna Ab Initio Simulation Package (VASP) is the computer program used to perform our first principles DFT calculations. The program has incredible depth and

there is significant documentation available online[1]. The software is regularly updated (calculations in this paper were performed using either VASP version 5.3.3 or 5.3.5, released in 2012 and 2014 respectively). VASP is often installed onto computing clusters, allowing multiple calculations to be performed simultaneously or a single calculation to be parallelized across multiple processors.

VASP requires a minimum of four input files: INCAR, KPOINTS, POSCAR, and POTCAR. The INCAR file contains most of the setting for a calculation, which are denoted in the form of capitalized INCAR "tags" (or "flags"). There are many flags, all with descriptions and options detailed in the VASP manual. Below are detailed the important INCAR flags used in these calculations, examples in the case of calculating an fcc-Co structure, and a description of their use:

SYSTEM =	Co_FCC	The system name appears in various output files.
PREC =	Normal	Influences the precision of the calulations. "Accurate" is critical for phonon calculations.
ENCUT =	400	The energy cutoff for the system; generally 1.5*ENMAX (found in the POTCAR files). Increasing this only increases computational time, while decreasing this can cause cutoff errors.
LREAL =	.FALSE.	Determines if the calculations are performed in reciprocal space (false) or real space (true). All calculations in this these performed in reciprocal space.
ISMEAR =	1	Always stayed at "1" for these calculations.
SIGMA =	0.2	Always stayed at "0.2" but it is important to set SIGMA such that T×S <1 meV/atom (see Starting Structures subsection).
NSW =	0	The number of ionic relaxation steps. "0" entails a "static run" , where no ionic relaxation will take place. For non-zero values, this serves as the maximum number of ionic relaxation steps performed before the calculation stops.
IBRION =	2	Determines how ions are updated and moved: "2" was always used in these calculations.
ISIF =	3	Determines which degrees of freedom are allowed to change. "3" allows the most freedom: ions can relax, and both the cell shape and cell volume can change.

[1]https://www.vasp.at/index.php/documentation

ISPIN =	2	Performs spin-polarized calculations. This is essential for systems that may have intrinsic magnetic moments, such as cobalt alloys. Increases computational time, but does not change end results for calculations that do not require spin-polarization.
MAGMOM =	3*2	3*(number of ions).
EDIFF =	1.0E-4	The allowed error in the total energy needed for electronic-step convergence. For high precision calculations, "1.0E-7" was used.
IALGO =	38	Determines the algorithm used to optimize the band structure. Many of the larger structures required "48" to be used to avoid critical errors.

The POSCAR file contains the lattice vectors and atomic positions for the starting structure. The format and description is given for the primitive B2-CoAl structure:

B2-CoAl	Name.
1.00	The scaling factor for the cell.
2.86 0.00 0.00	
0.00 2.86 0.00	Lattice vectors.
0.00 0.00 2.86	
Co Al	Elements of the structure.
1 1	Number of each element.
Direct	The atoms are placed at fractions of the lattice vectors.
0.00 0.00 0.00	Co is placed at the origin.
0.50 0.50 0.50	Al is placed at the center of the cell.

The KPOINTS file determines the reciprocal lattice grid upon which calculations are performed. The format and description for a B2-CoAl structure:

k-points for CoAl	Name.
0	Sets the k-points to be generated automatically.
Gamma	The grid with be centered at the Gammapoint in reciprocal space. Used for all these calculations.
9 9 9	Number of grid spacings in each direction.
0 0 0	Allows the mesh to be shifted. Always zeros in these calculations.

The POTCAR file contains the pseudopotential data for the DFT calculations. All these calculations were performed using projector augmented wave (PAW) potentials with parameters from Perdew, Burke, and Ernzerfhof (PBE). For structures with multiple

elements, the individual POSCARs are concatenated based on their order in the POSCAR file.

2.b Starting Structures

The six important structures in these initial investigations are hcp-Co, fcc-Co, B2-CoAl, $D0_{19}$-Co_3W , bcc-W, and fcc-Al. Each phase's crystal structure and experimental lattice parameters can be found from various sources, with an especially useful reference being the Materials Project[5]. It can be useful to build these structures using visualization tools such as VESTA[2]. Also, it is important that the structures be in their *primitive* form. For example, the conventional and primitive POSCARs for fcc-Co are given below:

Co_FCC conventional	Co_FCC primitive
1.00	1.00
3.52 0.00 0.00	0.00 1.76 1.76
0.00 3.52 0.00	1.76 0.00 1.76
0.00 0.00 3.52	0.00 0.00 3.52
Co	Co
4	1
Direct	Direct
0.00 0.00 0.00	0.00 0.00 0.00
0.00 0.50 0.50	
0.50 0.00 0.50	
0.50 0.50 0.00	

Using the primitive form minimizes errors and aids in manipulating the structure in future calculations.

Choosing the correct number of k-point grid spacings is essential for ensuring sufficient precision. A k-points convergence test should be performed for every primitive structure. This involves running a number of static calculations (NSW=0) with increasingly larger values of k-point spacing. As seen in Figure 5, the energy for CoAl converges to a value of -6.030 eV/atom at sufficiently high numbers of k-points. The k-point grid is deemed converged when the energy difference between different successive k-point runs is <0.5 meV/atom. This ensures that any calculations will be independent of the number of

[2]http://jp-minerals.org/vesta/

k-points chosen. During these calculations, it is important to keep the entropy low. While DFT calculations are meant to take place at 0K, numerical concerns determine that the calculations are performed at slightly elevated temperature then shifted back to 0K. The >0K entropy present (T×S) should be small, and is determined by the smearing parameter (INCAR flag SIGMA). This manifests itself in the energy difference between the calculated energy and the shifted energy (F vs E0 in the OSZICAR energy output file). The value of T×S should remain <1 meV/atom. SIGMA=0.2 was sufficient in all these calculations.

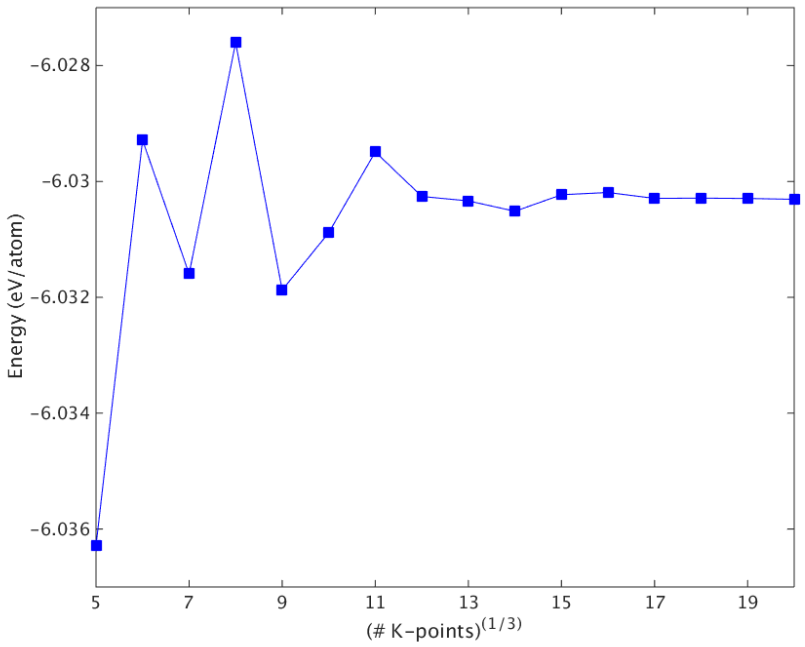

Figure 5: K-point convergence test for CoAl. A k-point grid with 3375 (15^3) k-points was chosen for high precision calculations.

K-point selection is more complicated in structures with non-cubic symmetry. The reciprocal lattice vectors in k-space are the inverse of the real-space lattice vectors, so the ratio between k-point spacings in each direction should be the inverse of the real-space ratios. For example, the $D0_{19}$-Co_3W structure has a hexagonal unit cell with lattice constants $a = 5.1\mathring{A}$ and $c = 4.1\mathring{A}$, resulting in a ratio $\frac{c}{a} = 0.8$. A good choice for the

k-point grid spacings would be 8×8×10. The result should be a k-point grid that has roughly equal reciprocal-length spacing in each direction.

2.c VASP Relaxation

To find the true ground state energy of a structure, it must be fully "relaxed". With full freedom of movement (ISIF = 3), VASP can nudge the atoms in a structure to achieve a lower energy state. When allowed to relax (NSW>0), the structure can converge to the lowest energy state where there are no residual forces. Some structures, especially structures with a large number of atoms, can take many ionic steps to converge (10-100+). Structures should be successively re-relaxed until they converge in only three ionic steps. Then a static run is performed to get the ground state energy.

Sometimes, fully relaxing a structure can result in breaking the symmetry of the crystal. Structures that are unstable may relax down to a more stable orientation. However, any mechanically stable structure should relax to its ground state, even if it is thermodynamically metastable (ex. fcc-Co metastable above hcp-Co). Some structures may not converge for various reasons. In this case, an alternative relaxation algorithm can be tried (IBRION tag), or the original POSCAR file may need to be reevaluated.

2.d Formation Energies

The ground state energies outputted by VASP need to be converted into formation energies. The formation energy is the energy difference between a compound and its constituent elements alone; a stable compound will have a negative formation energy. For our ternary system, the equation for formation energy is:

$$E_f(x_{Al}, x_W) = E_0(x_{Al}, x_W) - x_{Al}E_0^{Al} - x_W E_0^W - (1 - x_{Al} - xW)E_0^{Co} \quad (1)$$

where x_{Al} and x_W are the atomic fractions of Al and W, and E_0^{Al}, E_0^W, and E_0^{Co} are the ground state energies for fcc-Al, bcc-W, and hcp-Co respectively. The single-element, 0K stable structures of fcc-Al, bcc-W, and hcp-Co that make up the endpoints of the ternary phase diagram naturally have a formation energy of zero. Different ways of performing DFT calculations may result in a systematic shift in the ground state energies, so using formation energies ensures reliable comparison. The ground state energies and formation energies for the important phases are given below:

Table 2: Energies for phases in the Co-Al-W system, meV/atom. Also comparison to published calculations.

	Ground state	Formation calculated	Formation [5]
hcp-Co	-7 108	0	0
fcc-Co	-7 089	19	20
fcc-Al	-3 745	0	0
bcc-W	-13 013	0	0
B2-CoAl	-6 031	-604	-603
$D0_{19}$-Co_3W	-8 665	-80	-81

The convex hull is the energy surface that connects the stable structures in compositional space. For this ternary system, and in the compositional domain relevant to this paper, the convex hull exists as a plane connecting hcp-Co, B2-CoAl, and $D0_{19}$-Co_3W . This means that the lowest energy state within this domain is a three phase mixture of hcp-Co, B2-CoAl, and $D0_{19}$-Co_3W .

3 $L1_2$ Pseudobinary & Cluster Expansion

3.a Methods

From the experimental phase diagram of the Co-Al-W ternary system, Figure 3, we expect that the all-important γ' phase may only be stable in a small region of compositional space. The $L1_2$ structure has two sublattices: the corner atoms and the face centers.

The composition of the $L1_2$ phase found experimentally predicts that there is Al or W at the corners with some solubility of Co on these sites. This corresponds to the shaped region of Figure 6. To start out, it is much easier probe along a pseudobinary line, where the corner lattice sites are restricted to hold only Al or W (the dotted line in Figure 6. Figure 4 shows the unit cell of this pseudobinary $L1_2$ structure which will have varying amounts of Al and W in the corner positions. Thus, the initial goal is to obtain the formation energies for the $L1_2$-Co_3(Al,W) pseudobinary, and compare it to the convex hull formed by the fcc-Co, $D0_{19}$-Co_3W , and B2-CoAl phases.

There are an infinite number of unique configurations that have the $L1_2$ structure and exist along this pseudobinary line. Two different structures that have the same composition may have vastly different energies due to their local ordering. The solution to this problem comes to us through statistical mechanics: macroscopic thermodynamic properties are linked directly to the energy of microstates through a partition function. For example, at constant T, P and concentration, the Gibbs free energy is $G = -kT\ln Q$, where the partition function

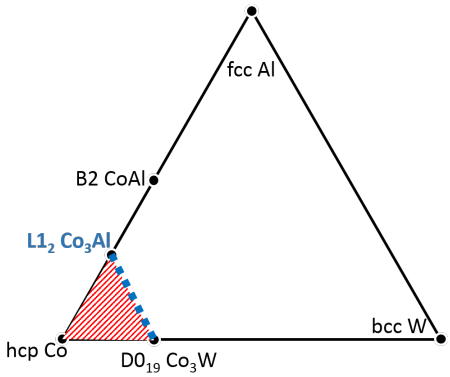

Figure 6: Schematic Co-Al-W ternary phase diagram showing the important phases. The shaded region indicates the compositional space where the $L1_2$ structure may occur. The dotted line shows the $L1_2$-Co_3(Al,W) pseudobinary line.

$$Q = \sum_s exp\left(\frac{-E_s}{k_B T}\right) \tag{2}$$

This sum is over all accessible microstates and E_s is the energy of a particular microstate, s. These microstates exist in every degree of freedom available to the system, which can include configuartional, vibrational, electronic, magnetic, strain, or others. Two important papers by Anton Van der Ven [6] [7] describe cluster expansion Hamiltonians

and their use in thermodynamic and kinetic simulations. These effective Hamiltonians use the DFT results from a limited number of microstates to predict the energy of any other microstates within the given degrees of freedom. Monte Carlo simulations can then be performed on these effective Hamiltonians in order to calculate thermodynamic averages by sampling a large number of microstates. A thorough understanding of this topic should be gained by reading the two papers above.

The CASM program enables the use of these effective Hamiltonians and Monte Carlo simulations in a highly automated fashion. CASM documentation details the use of the code, but an overview of the steps used to perform these specific calculations is given here. The three initial files required are the PRIM, SPECIES, and CSPECS. The PRIM is the primitive unit cell that will be manipulated to generate microstates/supercells. Its structure is almost identical to a POSCAR. For the $L1_2$-Co_3(Al,W) pseudo-binary cluster expansion, the PRIM is given below:

Gamma_prime Co3(Al,W)	Name
1.000	Scaling factor
3.576 0.000 0.000	
0.000 3.576 0.000	Lattice vectors
0.000 0.000 3.576	
1 3	Number of each species
Direct	
0.000 0.000 0.000 Al W	This lattice site is a configurational degree of freedom, occupied by either Al or W
0.000 0.500 0.500 Co	Lattice coordinate occupied by Co
0.500 0.000 0.500 Co	Lattice coordinate occupied by Co
0.500 0.500 0.000 Co	Lattice coordinate occupied by Co

This primitive cell was created by building an $L1_2$ 2x1x1 supercell (eight atoms, $Co_6Al_1W_1$) and fully relaxing it to get the primitive lattice parameters. A 9×9×9 k-point grid was chosen based on a k-point convergence test. The SPECIES file contains the atomic masses and starting guesses for the magnetic moments, used to generate the proper INCAR files:

	Al	W	Co
mass	26.982	183.84	58.933
magmom	0	0	2.0

The CSPECS file establishes the cutoff radii for the cluster functions used to fit the effective Hamiltonian:

Gamma Prime cluster size	within sphere radius	Name
2	15.0	Cutoff radius for pair clusters
3	12.0	Cutoff radius for triplet clusters
4	10.0	Cutoff radius for quadruplet clusters clusters

These CSPECS parameters resulted in one point cluster (the Al-W sublattice site), 17 pair clusters, 75 triplet clusters, and 100 quadruplet clusters; this is sufficient for a good fit to the effective Hamiltonian in a binary system. From here, CASM is used to generate 3-dimensional supercells up to a certain size (contained in the "SCEL" file) and the resulting configurations that can be made from these supercells (in the "configuration" file). Using clusters to generate structures removes the structures that are symmetrically equivalent, resulting in unique structures being used to fit the effective Hamiltonian. Supercells up to size six (24 atoms) were generated, resulting in 143 unique configurations spread across 13 different compositions (including the endpoint structures, Co_3W and Co_3Al). The CASM code automatically generates the necessary INCAR, KPOINTS, and POTCAR files for each configuration (based on the respective files from the primitive cell).

3.b Configurations

The 143 unique configurations were relaxed until their energy converged. If any configurations could not converge they would have been thrown out, but that did not occur in these calculations. All the configurations were checked to ensure that they retained their fcc-related symmetry, and had not relaxed to a different crystal structure. The formation energies were calculated based on Equation 1, and are plotted in Figure 7a. Also plotted in Figure 7a is the line created by the convex hull intersecting the pseudobinary.

If any configurations fall below this line, "breaking" the convex hull, then the $L1_2$ phase is stable in that configuration. However, all the $L1_2$ configurations lie above this line, so the lowest energy state along this pseudo-binary is a three-phase mixture of hcp-Co, B2-CoAl, and $D0_{19}$-Co_3W .

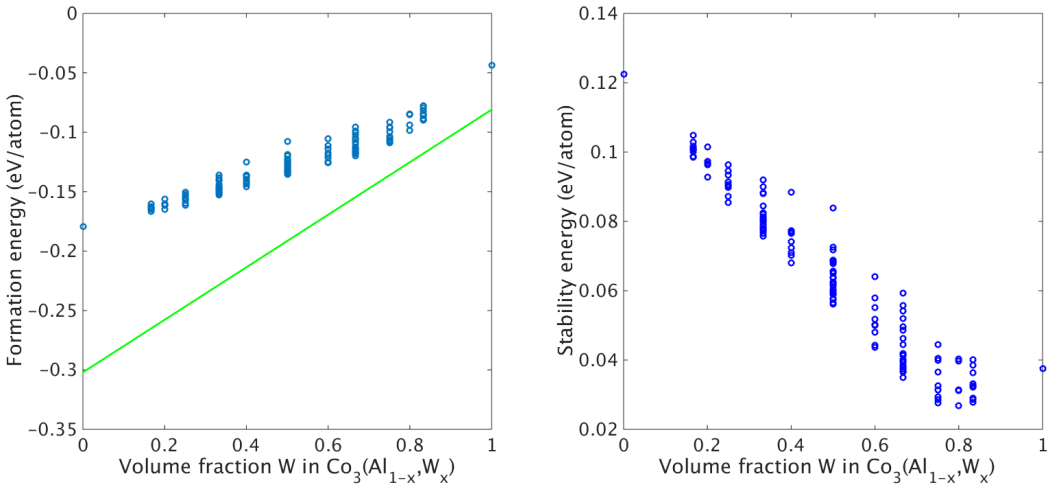

(a) (b)

Figure 7: (a) Formation energies for the 143 $L1_2$ configurations; the line indicates the pseudo-binary intersection with the convex hull. (b) Stability energy for the 143 $L1_2$ configurations.

In our quest to find an $L1_2$ structure that is stable, it use useful to define a new energy term that describes the energy difference between the $L1_2$ phases and the convex hull. This "stability energy" is defined below and plotted in Figure 7b:

$$E_{stab}(x_W) = E_f(x_W) - \frac{1}{2}(1 - x_w)E_f^{CoAl} - x_W E_f^{Co3W} \tag{3}$$

where x_W is the volume fraction in $Co_3(Al_{1-x}, W_x)$ and E_f^{CoAl} and E_f^{Co3W} are the formation energies for B2-CoAl and $D0_{19}$-Co_3W respectively. More generally, the stability energy in the ternary system is given by

$$E_{stab}(x_W, x_{Al}) = E_f(x_W, x_{Al}) - 2x_{al}E_f^{CoAl} - 4x_W E_f^{Co3W} \tag{4}$$

where x_W and x_{Al} are the volume fractions in $Co_{1-xW-xAl}(Al_{xAl}, W_{xW})$. From Figure 7b, we can see that most stable structure is on the W-rich side of the pseudobinary line, and is only ~ 25 meV/atom above the convex hull. This is an interesting result because the γ' phase tends to appear experimentally with almost equal amounts of Al and W.

3.c Hamiltonian fitting & Monte Carlo

The coefficients that make up the Hamiltonian require fitting from the energy of the individual structures calculated in DFT. It must be determined which basis functions of the cluster expansion are significant to include, and then the coefficients must be determined by a least-squares fit. The important basis function coefficients are referred to as effective cluster interactions (ECIs). The fitting process is performed by a genetic algorithm[8] that determines the optimal set of cluster expansion basis functions and fits them. The fitness of the genome produced by the genetic algorithm is judged by its cross-validation (CV) score [9]. It is the average error of the predicted energy for an excluded configuration,

$$CV^2 = \frac{1}{N}\sum_{i=1}^{N}\left(\tilde{E}_i - E_i\right)^2 \tag{5}$$

where E_i is the formation energy of configuration i, and $\tilde{E}_i$ is the energy predicted for configuration i by the fitted Hamiltonian with configuration i excluded. A properly performed genetic calculation results in a low CV score, i.e. a cluster expansion that is able to predict any given structure's energy with a high degree of accuracy. Running the

genetic optimization algorithm resulted in a final basis set comprised of 25 clusters with the CV score of the ECIs being 0.45 meV/atom. This resulting basis set consisted of zero-order, first-order, two pair, 10 triplet, and 11 quadruplet clusters.

Since we are now able to calculate a structure's energy with low computational cost by using the fitted Hamiltonian, the next step is to perform Monte Carlo simulations to determine the macroscopic thermodynamic properties. The MC simulations are performed between -100 and 1500°C in increments of 100°C. The calculations add alloying additions of Al and W in a 12×12×12 simulation cell, with the energies calculated by using the cluster expansion. The chemical potential data is obtained once MC energetic equilibrium is achieved. This chemical potential is integrated across concentration, resulting in free energy. This configurational energy componenent at finite temperature is an important contribution to the total energy landscape. However, at 0K, the smooth configurational energy curve is not much lower than the individual structures shown in Figure 7a. Since line compounds have no configurational entropy, the fcc-Co, B2-CoAl, and $D0_{19}$-Co_3W phases cannot be compared at nonzero temperature yet. In order to compare the relative stabilities of all the phases at elevated temperature, the vibrational energy component of the total energy must be calculated for all phases of interest in the system.

In experiments, we know that the $L1_2$ structures are only potentially stable in a small range of elevated temperatures. In order to explore this system at higher temperature, the energy contribution due to lattice vibrations must be included in our calculations. This energy contribution can have a large effect on the relative stability between phases. As seen in the next section, vibrational calculations are based off the primitive cell of a phase. But these $L1_2$ structures exist across a range of concentrations and innumerable structures. In order to calculate the vibrational energy contribution that the $L1_2$-Co_3(Al,W) structures experience, the endpoints of the pseudo-binary line are chosen as primitive $L1_2$ structures. The vibrational energy contribution may be different between the $L1_2$-Co_3Al

and $L1_2$-Co_3W structures, so the assumption is made that the vibrational energy of any structure on the pseudobinary line is derived from the rule of mixtures. That is,

$$F_{vib}(x_W, T) = x_W F_{vib}^{L1_2-Co_3W}(T) + (1 - x_W) F_{vib}^{L1_2-Co_3Al}(T) \tag{6}$$

3.d Results

From statistical mechanics, we can calculate an upper limit for the magnitude of the configurational energy contribution in the $L1_2$-Co_3(Al,W) structures:

$$G_{mix}(T) = \frac{1}{4} k_B T \sum_i x_i \ln(x_i) \tag{7}$$

where x_i is the atomic fraction of species i on the B sublattice of $L1_2$, in this case Al and W. The comparison between the calculated and upper limit for the configurational energy is shown in Table 3. These numbers show that the $L1_2$ structures will be stabilized by configurational energy, but alone will not be enough to render $L1_2$ stable relative to the convex hull.

Table 3: Ideal vs calculated configurational energies at different temperature for the $Co_3Al_{0.5}W_{0.5}$ structure.

Temperature	Ideal Configurational Energy	Calculated Configurational Energy
(°C)	(meV/atom)	(meV/atom)
0	0.0	0.0
300	-8.6	-4.5
600	-13.0	-8.6
900	-17.5	-12.9
1200	-22.0	-17.2

4 Vibrational Energy - Phonons

4.a Theory

The vibrational energy carried by phonons in a material can be a significant portion of a phase's internal energy at elevated temperature. The simplest analysis regarding phonons is called the harmonic approximation and assumes that an atom undergoing motion in a phonon experiences a restoring force that is proportional to its displacement. The derivation of the harmonic approximation is given below and is used to obtain the Helmoltz free energy: the free energy at constant volume.

Summarizing from Kundu [10], the Hamiltonian of a vibrating crystal is given by

$$H = \sum_{nli} \frac{M_n}{2} \dot{u}_i^2(n,l) + \frac{1}{2} \sum_{nli} \sum_{ml'j} \phi_{ij} \begin{pmatrix} m, & n \\ l, & l' \end{pmatrix} u_i(n,l) u_j(m,l'), \tag{8}$$

where the first summation is the kinetic energy, the second summation is the potential energy, and

$$\phi_{ij} \begin{pmatrix} m, & n \\ l, & l' \end{pmatrix} = \left(\frac{\partial^2 U}{\partial u_i(n,l) \partial u_j(m,l')} \right)_0 \tag{9}$$

Here, M_n is the mass of the n^{th} atom, $u_i(n,l)$ is a small displacement of the n^{th} atom in the l^{th} cell along the i^{th} direction, i, j represent components of the Cartesian coordinate axes and U is the ion-ion interaction potential. Moreover, $\phi_{ij}(m,n;l,l')$ is defined as the force acting on the n^{th} atom in the l^{th} cell along the i^{th} direction due to a displacement of the m^{th} atom in the l'^{th} cell along the j^{th} direction. From Newton's second law, the equation of motion of the n^{th} atom in the l^{th} cell is given by

$$M_u \ddot{u}_i(n,l) = - \sum_{ml'j} \phi_{ij} \begin{pmatrix} m, & n \\ l, & l' \end{pmatrix} u_j(m,l'). \tag{10}$$

We can see that by displacing atoms and then calculating the resulting force matrix acting on other atoms in the cell (ϕ_{ij}), we can set up a force balance. From the translational symmetry of a crystal the small displacement can be written as

$$u_i(n,l) = M_n^{-\frac{1}{2}} u_{in} \exp[i\vec{k} \cdot \vec{R}_n(l)] \tag{11}$$

where u_{in} is the amplitude of vibration along the i^{th} direction of the n^{th} atom, ω is the angular frequency, k is the wave vector, and $\vec{R}_n(l)$ is the position of the n^{th} atom in the l^{th} cell. Further,

$$\omega^2 u_{ni} = \sum m, j D_{ij}(mn,k) u_{mj} \tag{12}$$

$$\text{where } D_{ij}(mn,k) = (M_m M_n)^{-1/2} \sum_l \phi_{ij} \begin{pmatrix} m, & n \\ l, & l' \end{pmatrix} exp(-i\vec{k} \cdot \vec{R}_n(l)) \tag{13}$$

is the dynamical matrix which contains all the information regarding the vibration of the lattice. As seen in Equation 13, the dynamical matrix is the Fourier transform of the force constants, with the square of the eigenvalues of this matrix giving the frequency of the normal modes of oscillation in the crystal.

The thermodynamic properties are calculated from the frequencies. It is useful to summarize the information from the dynamical matrix by calculating the phonon density of states, which gives the number of modes of oscillation having a frequency ν:

$$g(\nu) = \frac{1}{N} \sum_{m=1}^{3N} \delta(\nu - \nu_m). \tag{14}$$

It can be shown that the Helmholtz free energy of the system is given by [11]

$$\frac{F_{vib}}{N} = \frac{E^*}{N} + k_B T \int_0^\infty \ln \left[2 \sinh \left(\frac{h\nu}{2k_B T} \right) \right] g(\nu) d\nu \tag{15}$$

where $E*$ is the potential energy of the system at its equilibrium position and h is Planck's constant.

4.b Quasiharmonic approximation

Because the harmonic approximation is performed at constant volume, the calculations do not take into account thermal expansion. This shortcoming alters the true energy of the phases, especially at higher temperatures. At elevated temperatures, we know that a structure will want to hydrostatically expand, so the constant volume Helmholtz energy essentially has an artificial strain energy associated with it. At elevated temperatures, the expanded structure will have lower energy. The solution to this problem is the quasiharmonic approximation. This involves generating Helmholtz energy curves at non-equilibrium volumes and finding the lowest energy path with temperature, resulting in the Gibbs free energy curve. Mathematically, this is calculated as

$$G(T,p) = \min_{\mathrm{V}} \left[E_0(V) + F_{vib}(V,T) + pV\right] \tag{16}$$

where E_0 is the ground state energy and p is the pressure (zero in all these calculations). These Gibbs free energy curves will allow a more accurate comparison between phases at elevated temperatures.

The vibrational free energy is ultimately derived from the force-constant tensors (ϕ_{ij}). With a variety of simplifying assumptions, these force-constant tensors can be determined using a managable number of atomic perturbations[12][13]. Specific atoms are chosen to be perturbed slightly in a specific direction with the highest degree of dimensionality. This minimizes the number of DFT calculations required while maintaining an accurate result. This method requires the creation of a supercell from the primitive cell, with one atom in the supercell perturbed away from its equilibrium position. The force response of the atoms to the perturbation is calculated using DFT, with the resulting force-constant

tensor given by

$$F(i) = \phi_{ij} u(j). \tag{17}$$

The perturbation selection process is mostly automated by CASM, but supercell selection is dictated by the user. The next section details the full process of obtaining vibrational free energy data.

4.c Methods

A very well relaxed primitive cell is essential for producing an accurate result. Because calculations rely on determing the forces caused by just a small perturbation in a supercell, even just minute variations away from true equilibirum can cause spurious results. This requires high precision relaxation: INCAR tag PREC=ACCURATE and EDIFF=1.0E-7. The latter tag sets a very low tolerance for achieving convergence during the electronic relaxation steps. During minimization, errors in the energy are of second order in the minimization parameters, while the errors on the forces are of the first order. If any significant residual forces remain after relaxation, this can cause major errors in subsequent calculations. The force vectors are found at the end of the OUTCAR file and should, for a converged cell, have a magnitude of <1 meV/Angstrom. Forces on atoms due to the perturbations are around $\sim 10 - 50$ meV/Angstrom in our calculations, but will vary considerably with perturbation magnitude.

Careful thought must be put into constructing the supercells for vibrational calculations. Since the DFT calculations are based on an infinite crystal utilizing periodic boundary conditions, supercells must be sufficiently large such that the perturbed atom does not interact with itself. Ideally a very large supercell would be used, but the computation time increases rapidly with cell size. A supercell size convergence test should be performed for each phase. Supercell shape is also important: the supercells should be as

"cubic" as possible. This is trivial for structures with cubic supercells, but requires creativity for more complex geometries. A clever trick for finding the most cubic/spherical supercells is to find the surface area to volume ratio. If the cell is a parallelepiped defined by the lattice vectors $\vec{a}, \vec{b}, \vec{c}$, the surface area to volume ratio is,

$$\frac{SA}{V} = \frac{|\vec{a} \times \vec{b}| + |\vec{b} \times \vec{c}| + |\vec{c} \times \vec{a}|}{|\vec{a} \cdot (\vec{b} \times \vec{c})|} \tag{18}$$

The supercells chosen for our important phases are shown in Table 4.

Another factor in supercell generation is the choice of k-points. The k-point grid of the supercell should keep the same reciprocal space grid length as the k-point grid of the primitive cell. This requires that the supercell size divide the primitive k-point grid evenly. Keep in mind that the k-point grid must also pass a k-point convergence test. The k-point grids chosen are shown in Table 4.

Table 4: Supercell size specifications for phonon calculations.

	atoms/cell	prim k-grid	supercell size	supercell k-grid	total # atoms
hcp-Co	2	15×15×10	3×3×2	5×5×5	36
fcc-Co	1	21×21×21	3×3×3	7×7×7	27
B2-CoAl	2	15×15×15	3×3×3	5×5×5	54
$D0_{19}$-Co_3W	8	10×10×12	2×2×2	5×5×6	64
$D0_{19}$ -Co_3Al	8	10×10×12	2×2×2	5×5×6	64
$L1_2$-Co_3W	4	22×22×22	2×2×2	11×11×11	32
$L1_2$-Co_3Al	4	22×22×22	2×2×2	11×11×11	32

To start using CASM for vibrational energy calculations, a PRIM file is required. The PRIM is simply the CONTCAR file from the high-accuracy primitive cell relaxation. CASM will analyze the primitive cell and calculate prospective supercells and appropriate atomic perturbations (perturbations with the highest degree of dimensionality should be chosen). Next, the desired supercell is inputted and the perturbation magnitude is selected. A perturbation magnitude of 0.01 Angstroms was chosen for all structures (see Appendix A for an analysis of the perturbation magnitude). The CASM code will then generate the required supercells with their respective perturbations. The code

is generally good about choosing an appropriate number of perturbations to calculate, however, additional perturbations can be generated and included in the calculations if required.

Using VASP, the forces are calculated with a static run (NSW=0). As these supercells are large in size (27-64 atoms), have high density k-point grids, and are calculated with high precision and a small convergence cutoff, these calculations can be computationally taxing.

After forces are calculated in VASP, the CASM code is used to fit the force constants, generate the dynamical matrix, and ultimately produce thermodynamic data. These calculations require additional input files: KPOINTS_LINE and KPOINTS_MESH. In reciprocal space, each Bravais lattice has a unique Brillouin zone that is defined by its symmetry. In these Brillouin zones, there are lines of highest symmetry that trace out the irreducible Brillouin zone. The most interesting phonon information is captured by isolating the frequencies along these high-symmetry k-paths. Setyawan and Curtarolo [14] give the coordinates for the high symmetry points in the Brillouin zones of all 14 Bravais lattices. The KPOINTS_LINE file contains the coordinates for the k-point path. The KPOINTS_MESH file defines the k-point grid density of the Brillouin zone that is used to calculate the phonon density of states and the thermodynamic information. A grid dimension of 50×50×50 was chosen for the hcp-Co, fcc-Co, and B2-CoAl structures while a 30×30×30 grid was chosen for the $D0_{19}$-Co_3W , $D0_{19}$-Co_3Al , $L1_2$-Co_3W , and $L1_2$-Co_3Al structures.

The important outputs from these calculations are the dispersion curves, density of states, and thermodynamic data. The dispersion curve for fcc-Co is shown in Figure 8 and displays the three acoustic phonon modes for the structure. Since fcc-Co is a single element structure, it only has acoustic modes. In contrast, the dispersion curve for B2-CoAl is shown in Figure 9 and shows six total phonon modes. This follows the $3N$ rule, where N is the number of atoms in the primitive cell, and there will be three

acoustic modes and $3(N-1)$ optical modes. The three acoustic modes should always have zero frequency at the Γ point (the center of the Brillouin zone) and the three optical phonon modes in CoAl describe the interaction of the Co and Al atoms. All frequencies are positive, indicating a stable structure (see Appendix B for scenarios with negative frequencies).

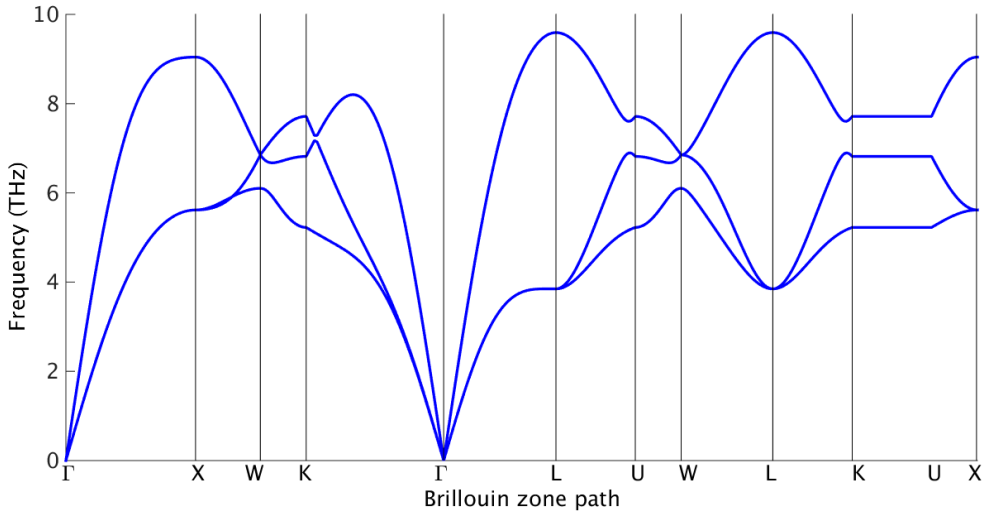

Figure 8: Dispersion curve for fcc-Co along the fcc Brillouin zone k-point path.

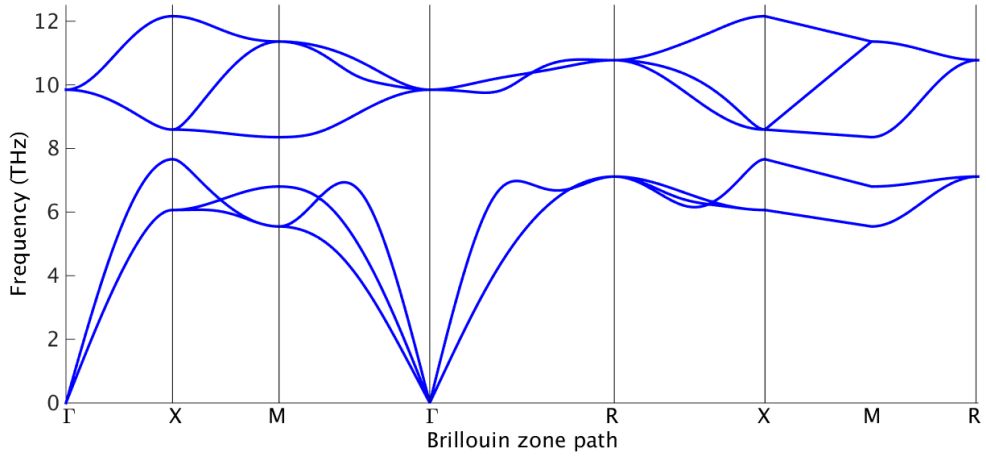

Figure 9: Dispersion curve for B2-CoAl along the simple cubic Brillouin zone k-point path.

When the frequencies in the Brillouin zone are integrated across their frequency do-

main, the result is a density of states (DOS) (Equation 14). This DOS can also be separated into its consituent parts by projecting the eigenvector of each basis atom onto the DOS, resulting in the partial density of states. Figure 10 shows the partial DOS for B2-CoAl. It shows that most of the Co-derived frequencies happen at lower frequencies, while the Al-derived frequencies occur at higher frequencies. This is likely due to aluminum's much lower atomic mass resulting in higher frequencies. Summing the two partial DOS together reveals the total DOS for CoAl. This DOS is used to generate the finite temperature thermodynamic information.

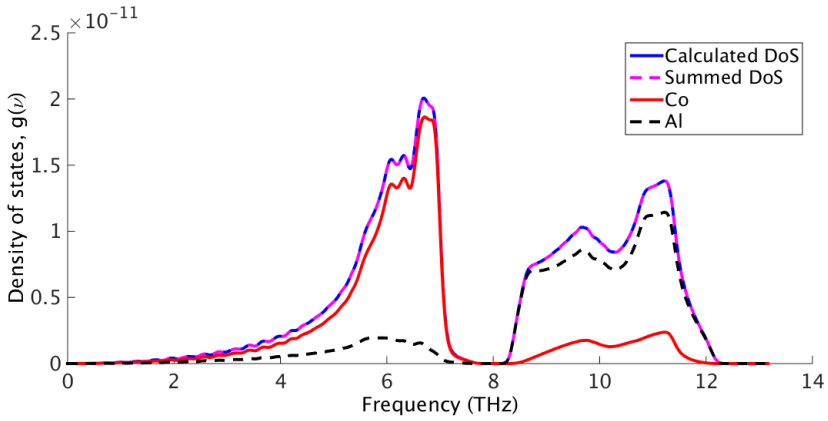

Figure 10: Partial and total phonon density of states for B2-CoAl.

The energy that results from these calculations is the constant volume Helmholtz energy. This includes the zero point energy present at 0K, so the starting energy is positive but decreases monotonically and is concave down with increasing temperature. Also calculated is the heat capacity and the vibrational entropy as a function of temperature.

4.d Gibbs Free Energy Calculations

Calculating the Gibbs free energy curves requires about $\times 10$ more computational time. Helmholtz energy curves must be created at a variety of non-equilibrium volumes. The primitive cells are first scaled to the desired non-equilibrium volumes. These cells must then be relaxed, allowing for small changes in cell shape and ion position, but *no* changes

in cell volume (INCAR tag ISIF=4). It is critical that the residual forces in these cells are negligible. If the cell relaxes a large amount, to a different crystal structure, then the scaled cell is likely mechanically unstable and the system may experience a true structure transition at this volume. However in some calculations, small relaxations occur in scaled structures. In some cases, the slightly relaxed cells broke the symmetry of the primitive cell. This is a tolerance issue in CASM and was solved by increasing the global tolerance. This caused CASM to consider the scaled cells to have the same symmetry as the equilibrium cells, which is essential for calculating the quasiharmonic approximation. The scaled cells are then used to created supercells with the same perturbations as the equilibrium cell. For example in $D0_{19}$-Co_3W , Helmholtz energy curves were calculated for nine volumes. These were -2% to +6% of the equilibrium volume, in intervals of 1%. If these energies are plotted as a function of volume at a specific temperature, Figure 11 is the result. These energy versus volume curves fit nicely to a parabola. By a least-squares regression, a smooth energy curve can be fit for energy vs volume at each temperature, thus creating our $F_{vib}(V,T)$ energy landscape. By applying Equation 16 and minimizing the energy with respect to volume, the lowest energy path across this energy landscape can be found, producing the Gibbs free energy curve.

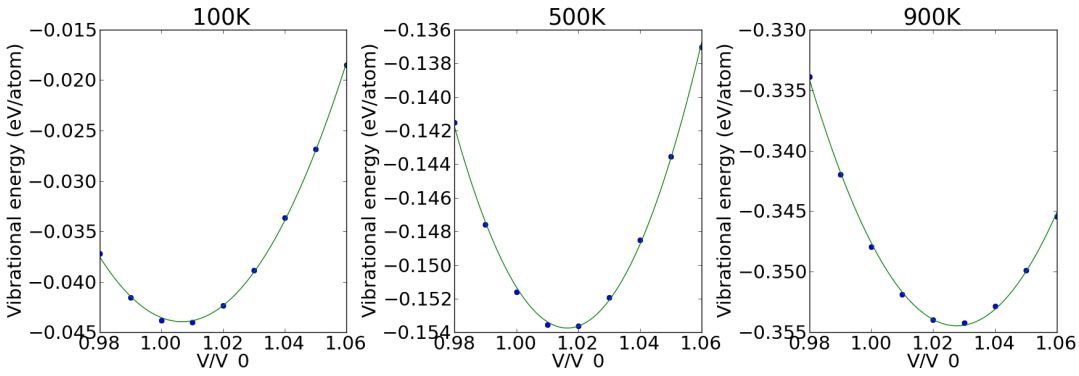

Figure 11: Helmholtz energy vs volume for $D0_{19}$-Co_3W at 100K, 500K, and 900K. The individual data points are plotted along with the fitted parabola.

Because the energy vs volume data fits to a parabola, the volume with temperature increases linearly, i.e. a constant coefficient of thermal expansion. The calculated

coefficients of thermal expansion are given in Table 5,

4.e Relative Vibrational Energies

The vibrational contribution to the Gibbs free energy curves for fcc-Co, B2-CoAl, and $D0_{19}$-Co_3W are shown in Figure 12a. This indicates how the relative stability of the phases changes with temperature. Fcc-Co and $D0_{19}$-Co_3W show similar temperature dependence, with fcc-Co being slightly more stable. B2-CoAl is significantly less stabilized by vibrational energy. (While the cause for this is unknown, it is an encouraging result because the formation energy of B2-CoAl is otherwise very low, so any destabilization of CoAl bodes well for the relative stability of the $L1_2$ phases.)

Table 5: Calculated coefficients of thermal expansion.

Phase	CTE(x10E-6/K)
hcp-Co	12.96
fcc-Co	12.87
B2-CoAl	10.08
$D0_{19}$-Co_3W	9.01

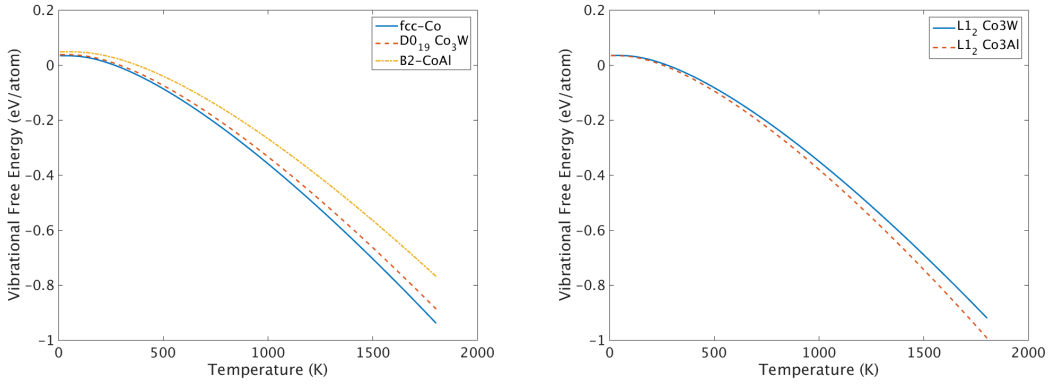

(a) (b)

Figure 12: Vibrational Gibbs free energy curves calculated from the quasiharmonic approximation for (a) fcc-Co, B2-CoAl, and $D0_{19}$-Co_3W and (b) $L1_2$-Co_3W and $L1_2$-Co_3Al .

Figure 12b shows the relative stability between the $L1_2$ endpoint structures. This shows that they start out at the same energy, but the $L1_2$-Co_3Al structure is more stabilized by vibrational energy as the temperature increases. This indicates that as the

temperature increases, Al-rich $L1_2$ structures will experience more stabilization relative to W-rich $L1_2$ structures. Comparing Figures 12a and 12b, we can see that the fcc-Co and the $L1_2$ phases are most stabilized by vibrational energy.

The Gibbs free energy difference between hcp-Co and fcc-Co is quite small at every temperature. The transition temperature where fcc-Co becomes stable occurs at 1190K according to these calculations. The experimental transition temperature is at 690K[4], significantly lower. Appendix C explains a possible reason for this difference.

5 Results: $L1_2$ stability

Combining the configurational and vibrational energy calculations together gives a much more complete picture of the energy landscape and allows us to compare the continuum of $L1_2$ structures to the convex hull composed of hcp-Co, B2-CoAl, and $D0_{19}$-Co_3W . This combined free energy as a function of tungsten composition and temperature is given,

$$G(x_W, T) = E_f^{L1_2}(x_W) + \int_0^{x_W} \mu_W dx_W + G_{vib}(x_W, T). \tag{19}$$

The energy fot the three line compounds looks similar, but omits the configurational energy term. As calculated in Equation 4, the stability energy of the $L1_2$ phases is their energy compared to the three phases at the corners of the convex hull. If the stability energy is negative, this indicates that the $L1_2$ structure is more stable than a three-phase mixture of hcp-Co, B2-CoAl, and $D0_{19}$-Co_3W . We know that at 0K, the lowest energy $L1_2$ structure has a stability energy of 27 meV/atom at a composition of $Co_3Al_{0.2}W_{0.8}$. As the temperature increases, the $L1_2$ structures become more stable compared to the hcp-Co, B2-CoAl, and $D0_{19}$-Co_3W phases. Figure 13a shows that the $L1_2$ phase becomes stable at 600°C . Above this temperature, the $L1_2$ phase continues to gain stability and the compositional domain of the stable $L1_2$ phase grows. At 900°C (Figure 13b), the most stable $L1_2$ exists at a composition of 69.5% W on the B sublattice, which is relatively

close to experimental findings.

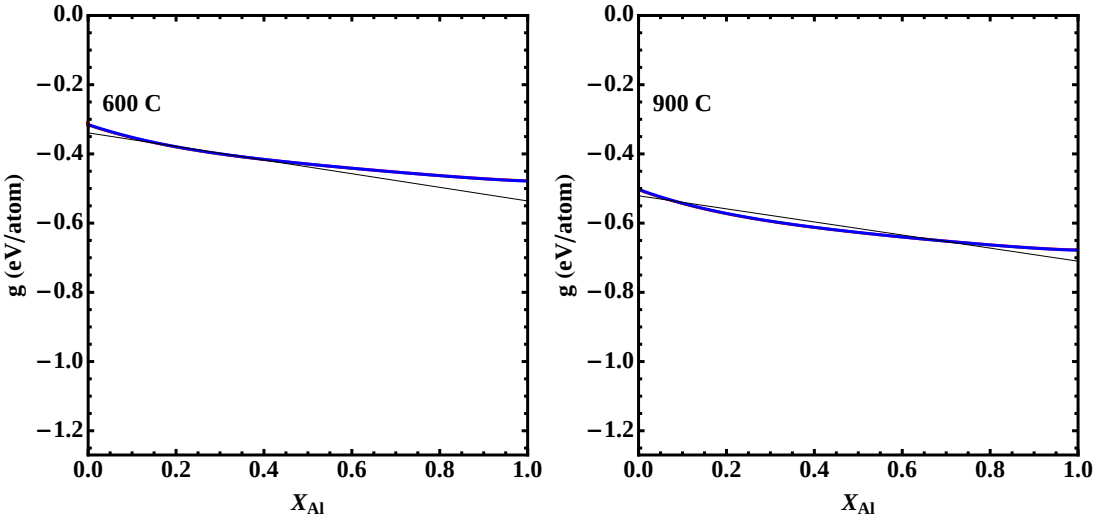

(a) (b)

Figure 13: $L1_2$ free energy vs the three-phase mixture of hcp-Co, B2-CoAl, and $D0_{19}$-Co_3W at (a) 600°C and (b) 900°C .

5.a Comparison to other works

No other simulations have found the $L1_2$ phases becoming stable relative to the three-phase mixture of fcc-Co, B2-CoAl, and $D0_{19}$-Co_3W . However, this is the first published study that includes both configurational energy in the form of a cluster expansion and vibrational energy results calculated using the quasiharmonic approximation. Both of these calculations increased the stability of the $L1_2$ phases relative to the three-phase mixture.

Saal and Wolverton [15] performed a first principles study on the Co-Al-W system. They calculated the formation energies and lattice vibration energies (in the harmonic approximation) for the important phases in the system. For the $L1_2$ phase, they used a special quasirandom structure (SQS) at a composition of $Co_3(Al_{0.5},W_{0.5})$. At 0K, the $L1_2$ SQS had an energy 66 meV/atom above the convex hull. They found that vibrational effects stabilized the $L1_2$ structure by 27 meV/atom at 1200K, a less dramatic effect than our results. With the inclusion of configuration entropy (-18 meV/atom) and the thermal

excitation of electrons (-10 meV/atom), the $L1_2$ structure was only 11 meV/atom above the convex hull at 1200K. Our calculations used the quasiharmonic approximation and used a cluster expansion rather than an SQS for our analysis, which could explain the discrepancy between our results.

Xu et al. [16] calculated lattice vibrational energy by the quasiharmonic phonon approach for the related $L1_2$ structures, Co_3(M,W) (M = Al, Ge, Ga). They, however, did not relate their results to the other important phases in their systems, so could not comment on the relative stability of the $L1_2$ phases. This study also calculated the energy contribution due to the thermal excitation of electrons, and found that it had a small effect on the total energy.

5.b Shortcomings & Future Work

There are assumptions made in these calculations that may effect the true nature of the energy landscape. First, the fcc-Co, B2-CoAl, and $D0_{19}$-Co_3W phases were considered line compounds. From Figure 3, it is obvious that this assumption is not true experimentally. The phase diagram indicates that while there is negligible solubility of the $D0_{19}$-Co_3W phase, there is some solubility of W and Al in the fcc-Co phase and a large amount of solubility of Co in the CoAl phase. Full calculations of the effects of this solubility on the energy is beyond the scope of this study, but preliminary calculations by Rob Rhein [17] indicate the effects of solubility in the B2-CoAl are negligible.

Second, the phonon calculations become less accurate at higher temperatures. High temperatures increase the importance of anharmonic effects, which could alter the stability energy.

Third, these calculations do not include energy contributions from the exitation of electrons at elevated temperature or other magnetic effects (beyond spin-polarization). While these contributions are likely to be much smaller than the configurational and vibrational components of free energy, they could still affect the relative stability.

Fourth, comparing experimental findings to calculated results is fraught with potential problems. These calculations do not include strain, kinetics, or the effects of trace alloying additions. Experimental results often contain non-equilibrium compounds, indicating that the energy difference between stable and metastable compounds may be slight. These caveats may explain the dramatic stability of our calculated $L1_2$ phase when compared to previous calculated results and experimental studies.

Future work will explore the Co-Al-W system in greater detail. This includes a ternary cluster expansion, rather than just a binary cluster expansion along the $L1_2$ pseudobinary line. This requires ternary cluster expansions in the full phase space for each expected structure: fcc, hcp, and bcc just to start. The ternary cluster expansions will give a much clearer picture of the true energy landscape, and better insight into where low energy structures may lie. Solubility should also be explored in phases that were treated as line compounds in this study.

It is also important to look at stabilizing alloying additions for the $L1_2$ structure. While the results in this paper are encouraging, work needs to be done to increase the phase space and temperature range where the γ-γ' microstructure can be created, as well as increasing the $L1_2$ solvus temperature. Based off the work in Ni-based superalloy development, experimental work is being performed in Co systems to look at the effects of Ta, Ge, Ga, Ti, Ni, and other elements. Computational work has already been performed on the effects of Ta [18] and other additions.

6 Conclusion

The results presented in this study indicate that a range of $L1_2$-Co_3(Al,W) structures are stable in the Co-Al-W system. By using first principles methods, formation energies were established for hcp-Co, fcc-Co, B2-CoAl, and $D0_{19}$-Co_3W structures. CASM, developed by the Anton Van der Ven group, was used to generate $L1_2$-Co_3(Al,W) structures along

the pseudobinary line between Co_3W and Co_3Al. These structures were used to create a cluster expansion and calculate the configurational energy contribution to $L1_2$ structures due to the solubility of Al/W on the $L1_2$ B sublattice. The vibrational energy contributions were calculated in the quasiharmonic approximation using the CASM code. The results show that the $L1_2$ structures first become stable relative to a three phase mixture of hcp-Co, B2-CoAl, and $D0_{19}$-Co_3W at 600K, and continue to become more stable with increasing temperature.

While these results are the first to indicate stability of the $L1_2$ structures, no previous calculations have been performed using both the quasiharmonic approximation and a cluster expansion. The stability of the $L1_2$ phase shows that Co-based superalloys are an encouraging alloy system for the development of high strength, high temperature materials.

A Perturbation Magnitude

The magnitude of the perturbation used to generate the phonon data can have a large effect on the results. The default perturbation magnitude is $0.01\mathring{A}$ because that is the magnitude chosen in many earlier works [19][9]. The $0.01\mathring{A}$ was chosen for silicon calculations, but is thought to work well for other metals and transition metals. For some applications much larger perturbations, on the order of $0.1\mathring{A}$, are needed.

To explore the effects of the perturbation magnitude, Gibbs free energy curves were constructed via the quasiharmonic approximation for hcp-Co and fcc-Co structures. Perturbation magnitude ranged from 0.01 to $0.04\mathring{A}$ in intervals of $0.01\mathring{A}$. The larger perturbations resulted in higher gibbs free energies, but the effects were very small: at 1200K, the $0.01\mathring{A}$ perturbation energy was only 1 meV/atom lower than $0.04\mathring{A}$ perturbation energy. When comparing the hcp-Co and fcc-Co energies, the changes in transition temperature were negligible.

These results indicate that the perturbation magnitude has little impact on the vibrational energy results in this system.

B Dispersion curves

The frequencies resulting from a phonon calculation *must* be positive for the data to be valid. This comes from the symmetry inherent to the crystal. From Kundu [10], the dynamical matrix is defined

$$D_{ij}(mn,k) = (M_m M_n)^{-1/2} \sum_l \phi_{ij} \begin{pmatrix} m, & n \\ l, & l' \end{pmatrix} exp(-i\vec{k} \cdot \vec{R}_n(l)). \tag{20}$$

This matrix is hermitian, i.e. $D_{ij} = D_{ji}^T$. This implies that the eigenvectors of the matrix are real and the resulting frequencies are positive. Non-trivial solutions for the matrix are obtained only if

$$|D_{ij}(mn,k) - \omega^2 \delta_{ij} \delta mn| = 0 \tag{21}$$

So imaginary eigenvalues and negative frequencies are only obtained if something goes wrong in the calculations. During the process of this report, a few structures showed negative frequencies, and required fixes.

The most common problem was small negative frequencies just around the gamma point. Since the magnitude of the negative frequencies were so small, this indicated that it was likely a numerical error. This problem was removed by increasing the electronic convergence threshhold (INCAR tag EDIFF to 1.0E-7) as well as ensuring that the supercell grid in the phonon calculations was "aligned" with the primitive cell grid. Accuracy issues could also be caused by too small of a k-point grid (not full converged), using a not fully relaxed primitive cell to construct the phonon supercells (residual forces in primitive cell should be $< 1meV/\mathring{A}$), or boundary effects from using too small of a phonon supercell.

Of more concern are phonon results that show large negative frequencies. Figure

14 gives an example of a dispersion curve for $D0_{19}$-Co_3Al that shows a large number of very negative frequency bands. This indicates that the structure is not mechanically stable. The $D0_{19}$-Co_3Al does not appear experimentally, so it is prone to relaxing to a different structure. The primitive cell in this case was relaxed using INCAR tag ISIF=7 which allows chance in cell volume but no change in cell shape or the position of atoms within the cell. This produced a structure that is not mechanically stable, and the atoms experience a force pushing them towards equilibrium even if a perturbation were not present. This causes the the severe distortions seen in Figure 14, as the calculations are indicating phonon modes that do not actually exist.

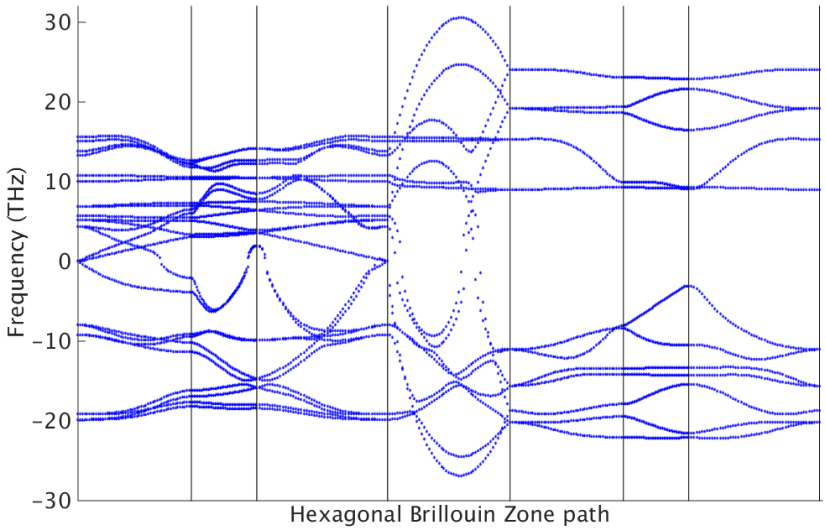

Figure 14: Dispersion curve for $D0_{19}$-Co_3Al created using a poorly relaxed primitive cell.

The solution to this problem was to relax the cell properly: until the residual forces were small. The residual forces in the cell were on the order of $10meV/\mathring{A}$, far too large to be considered converged. Allowing just a slight change in cell shape during relaxation caused the forces to drop to converged levels.

The dispersion curve shown in Figure 14 is dramatic, and most mechanically unstable cells will show fewer negative bands. It is always important to check the a primitive cell is converged and that the relaxed supercells have kept the same symmetry as the primitive cell.

C Magnetic Effects

Results from the Vibrational Energy section show that using the Gibbs free energy curves calculated using the quasiharmonic approximation result in a transition temperature at 1190K. Experimental results indicate that the transition temperature occurs at 690K [4]; significantly lower. The energy difference between hcp-Co and fcc-Co at 0K is 19

meV/atom according to our VASP calculations. This is quite a small amount of energy, which implies that small energy effects that are otherwise ignored may play a large role in the hcp-fcc transition.

Due to cobalt being a ferromagnetic element with an intrinsic magnetic moment, the alignment of magnetic moments plays an important role in its ground state energy (the reason for including spin-polarization in DFT calculations). In a ferromagnet, the spin of the electrons align to produce a net magnetic moment in one direction. We know that as ferromagnets are heated, their intrinsic magnetic moment decreases until it reaches the Curie temperature when the net magnetic moment goes to zero. The traditional theory is that thermal fluctuations cause some spins to flip into an antiferromagnetic orientation, reducing the net magnetic moment. A more complete theory breaks away from this binary view and introduces the idea of spin-fluctuations: individual magnetic moments having a two dimensional vector quality. What results are "spin spirals", where transition from "up spin" to "down spin" is shared over multiple atoms. Uhl & Kübler[20] used DFT to calculate the energies resulting from spin-fluctuations in hcp-Co and fcc-Co. They concluded that the hexagonal phase of Co is stabilized predominantly by its intrinsic magnetism, with spin fluctuations and the decreasing magnetization at higher temperatures restoring the natural tendency of cobalt to be fcc. Using solely the energy contribution from spin fluctuations, they found the transition temperature to exist at 590K. If we make the assumption that the relative fcc stabilization by spin-fluctuations goes linearly with temperature, we can calculate the spin-fluctuation energy contribution to be

$$E_{s-f}(T) = \frac{19meV/atom}{590K}(T) = 0.032\frac{meV}{atom * K}(T) \tag{22}$$

This energy contribution can be added to our quasi-harmonic energy calculations and produces a new hcp-fcc transition temperature of 780K. This result compares favorably to the experimental temperature of 690K and the 90K difference between our result and experiment represents 2.6 meV/atom of energy difference. This energy difference could be within the margin of error for our energy results coupled with Uhl & Kübler's calculations. Later papers cover spin-fluctuation theory in greater depth[21][22].

My own rudimentary results qualitatively match up with Uhl & Kübler's. I produced a variety of hcp and fcc Co supercells with differing degrees of antiferromagnetism, setting up a binary-spin cluster expansion. This was done by setting a value in the MAGMOM tag in the INCAR file to a negative value to represent an anti-ferromagnetic flip. These calculations are finicky because they disrupt some of the automatic variable-choosing in VASP. Sometimes the number of bands (NBANDS) is lower than it should be, resulting in skewed energy values. Most of the hcp Co structures did not converge due to errors that appeared and remain unresolved. My results indicate that the lowest energy state in fcc Co was ferromagnetic, and the energy increases with degree of antiferromagnetism up to the purely antiferromagnetic state. In order to calculate the Hamiltonian representing spin-fluctuations, the LSORBIT tag must be used in the INCAR file. This allows the spin axis to be changed. This is the method by which DFT can be used to fit the Hamiltonian and ultimately the energy landscape representing spin-fluctuations in a material.

References

[1] T. M. Pollock and S. Tin, "Nickel-based superalloys for advanced turbine engines: Chemistry, microstructure, and properties," *Journal of Propulsion and Power*, vol. 22, pp. 361–374, April 2006.

[2] J. Sato, T. Omori, K. Oikawa, I. Ohnuma, R. Kainuma, and K. Ishida, "Cobalt-base high-temperature alloys," *Science*, vol. 312, no. 5770, pp. 90–91, 2006.

[3] S. Kobayashi, Y. Tsukamoto, T. Takasugi, H. Chinen, T. Omori, K. Ishida, and S. Zaefferer, "Determination of phase equilibria in the co-rich coalw ternary system with a diffusion-couple technique," *Intermetallics*, vol. 17, no. 12, pp. 1085 – 1089, 2009.

[4] J. Giber, R. Drube, and V. Dose, "Critical point energies in hcp and fcc cobalt from appearance potential spectra," *Applied Physics A*, vol. 52, no. 2, pp. 167–170, 1991.

[5] A. Jain, S. P. Ong, G. Hautier, W. Chen, W. D. Richards, S. Dacek, S. Cholia, D. Gunter, D. Skinner, G. Ceder, and K. a. Persson, "The Materials Project: A materials genome approach to accelerating materials innovation," *APL Materials*, vol. 1, no. 1, p. 011002, 2013.

[6] A. Van der Ven, J. C. Thomas, Q. Xu, B. Swoboda, and D. Morgan, "Nondilute diffusion from first principles: Li diffusion in $\mathrm{li}_x\mathrm{tis}_2$," *Phys. Rev. B*, vol. 78, p. 104306, Sep 2008.

[7] A. V. der Ven, J. Thomas, Q. Xu, and J. Bhattacharya, "Linking the electronic structure of solids to their thermodynamic and kinetic properties," *Mathematics and Computers in Simulation*, vol. 80, no. 7, pp. 1393 – 1410, 2010. Multiscale modeling of moving interfaces in materials.

[8] G. L. W. Hart, V. Blum, M. J. Walorski, and A. Zunger, "Evolutionary approach for determining first-principles hamiltonians," *Nature Materials*, vol. 4, pp. 391–394, 2005.

[9] A. van de Walle and G. Ceder, "The effect of lattice vibrations on substitutional alloy thermodynamics," *Reviews of Modern Physics*, vol. 74, pp. 11–45, Jan 2002.

[10] R. Kundu, "Towards phonon spectrum of graphene," Feb 2008.

[11] A. A. Maradudin, E. W. Montroll, and G. H. Weiss, *Theory of Lattice Dynamics in the Harmonic Approximation*. Academic Press, 1971.

[12] S. Wei and M. Y. Chou, "Ab initio calculation of force constant and full phonon dispersions," *Physcial Review Letters*, vol. 69, November 1992.

[13] G. D. Garbulsky and G. Ceder, "Contribution of the vibrational free energy to phase stability in substitutional alloys: Methods and trends," *Phys. Rev. B*, vol. 53, pp. 8993–9001, Apr 1996.

[14] W. Setyawan and S. Curtarolo, "High-throughput electronic band structure calculations: Challenges and tools," *Computational Materials Science*, vol. 49, no. 2, pp. 299 – 312, 2010.

[15] J. E. Saal and C. Wolverton, "Thermodynamic stability of coalw {L12} ," *Acta Materialia*, vol. 61, no. 7, pp. 2330 – 2338, 2013.

[16] W. Xu, J. Han, Y. Wang, C. Wang, X. Liu, and Z.-K. Liu, "First-principles investigation of electronic, mechanical and thermodynamic properties of {L12} ordered co3(m, w) (m=al, ge, ga) phases," *Acta Materialia*, vol. 61, no. 14, pp. 5437 – 5448, 2013.

[17] R. K. Rhein, P. C. Dodge, M. S. Titus, A. Mottura, A. V. der Ven, and T. M. Pollock, "Vibrationally-induced stability of the $L1_2$ phase along the co3al-co3w pseudobinary line demonstrated using first principles methods," *Acta Materialia*, Pending publication.

[18] A. Mottura, A. Janotti, and T. M. Pollock, "A first-principles study of the effect of Ta on the superlattice intrinsic stacking fault energy of $L1_2$-Co_3(Al,W)," *Intermetallics*, vol. 28, pp. 138–143, 2012.

[19] W. F. Kuhs, "Generalized atomic displacements in crystallographic structure analysis," *Acta Crystallographica Section A*, vol. 48, pp. 80–98, Mar 1992.

[20] M. Uhl and J. Kübler, "Exchange-coupled spin-fluctuation theory: Application to fe, co, ni," *Physical Review Letters*, vol. 77, no. 2, pp. 334–337, 1996.

[21] J. Staunton, S. Razee, L. Szunyogh, and B. Gyorffy, "Theory of metallic magnetism at finite temperatures in bulk materials and thin films," *Physica B: Condensed Matter*, vol. 318, no. 4, pp. 316 – 320, 2002. Proceedings of the 6th Patras University Euroconference on Proper ties of Condensed Matter Probed with X-ray Scattering - Electron Correla tions and Magnetism.

[22] M. Ležaić, P. Mavropoulos, G. Bihlmayer, and S. Blügel, "Exchange interactions and local-moment fluctuation corrections in ferromagnets at finite temperatures based on noncollinear density-functional calculations," *Phys. Rev. B*, vol. 88, p. 134403, Oct 2013.